Supporting Information

High-thermoelectric power factor of Si-Mg_2Si nanocomposite ribbons synthesized by melt-spinning

Daiki Souda[a], Kazuto Shimizu[a], Yuji Ohishi[a], Hiroaki Muta[a], Takashi Yagi[b], and Ken Kurosaki[a, c, d, e, *]

[a] *Graduate School of Engineering, Osaka University, 2-1 Yamadaoka, Suita, Osaka 565-0871, Japan*

[b] *National Metrology Institute of Japan, National Institute of Advanced Industrial Science and Technology, Tsukuba, Ibaraki 305-8563, Japan*

[c] *Research Institute of Nuclear Engineering, University of Fukui, 1-3-33 Kanawa-cho, Tsuruga, Fukui 914-0055, Japan*

[d] *Institute for Integrated Radiation and Nuclear Science, Kyoto University, 2 Asashironishi, Kumatori-cho, Osaka 590-0494, Japan*

[e] *JST, PRESTO, 4-1-8 Honcho, Kawaguchi, Saitama 332-0012, Japan*

* Corresponding author: kurosaki.ken.6n@kyoto-u.ac.jp

Details of the TE properties measurements for ribbons.

Since the ribbon samples could not be set on ZEM-3 with its original form, a ribbon with approximately 20 mm length was fixed on an alumina substrate using conductive silver paste as shown in Figure S1(a). Then, the substrate was set on ZEM-3 as shown in Figure S1(b), which enables us to measure the TE properties of the ribbon. The measurement was performed in a reduced helium atmosphere.

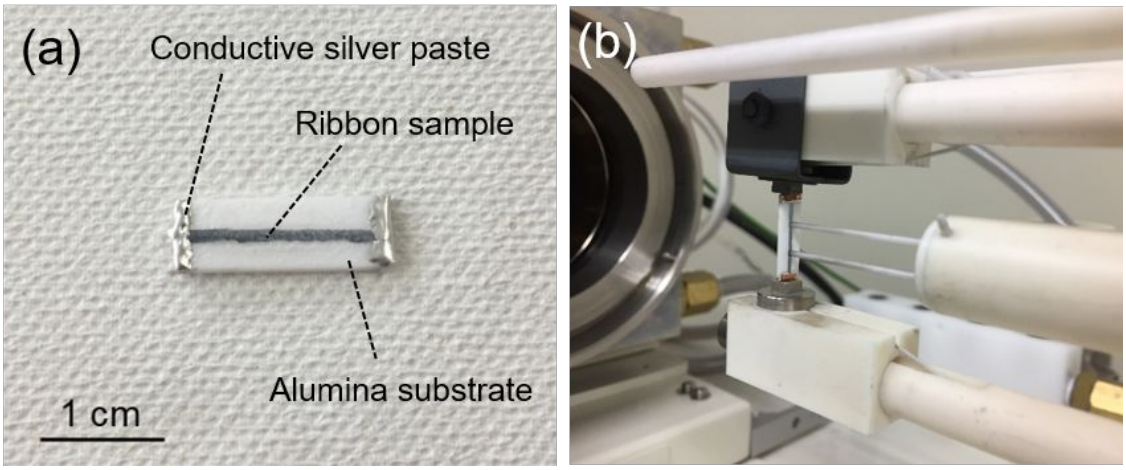

Figure S1. Experimental setup to measure the TE properties of a ribbon by using ZEM-3, (a) Appearance of the sample and (b) Sample setting inside ZEM-3.

The measurement setup of α is shown in Figure S2. An approximately 25 mm length of a ribbon was fixed on a cupper ring with the inner diameter of 20 mm, and those were set into a temperature controlled chamber (no drawing in the figure). Then, the center of the ribbon was periodically heated by a laser beam with the wavelength of 808 nm, power of 2 mW, frequency of 2 Hz, and spot diameter of 150 μm to generate modulated temperature field in the sample. Applied heat diffused parallel to the ribbon, so that one-dimensional heat diffusion was generated in the sample. A Ge lens positioned backside of the sample collects thermal radiation from the sample with a diameter of 150 μm to measure a phase delay between the temperature modulation and the heating laser. Moving the Ge lens along with the ribbon, we recorded the relation between the phase delay, θ and distance from the heating point, x at respective temperatures as shown in Figure S2. α can be derived using following relation:

$$\alpha = \pi f / \left(\frac{d\theta}{dx}\right)^2, \quad \text{(S1)}$$

where f is a frequency of the laser. In order to avoid chemical reactions at higher temperatures, we did not apply any black coating, which is often used to enhance thermal radiation.

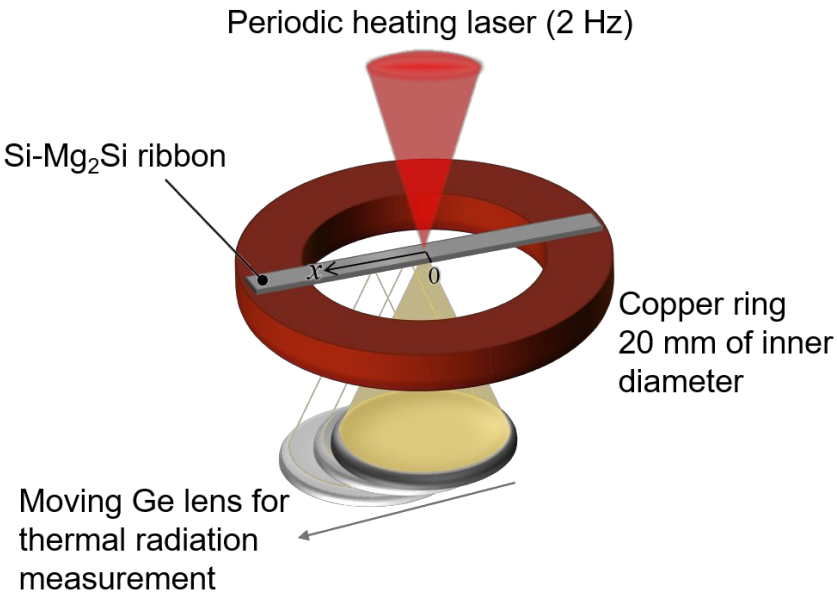

Figure S2. Measurement set up of thermal diffusivity based on a laser spot periodic heating radiation thermometry method.

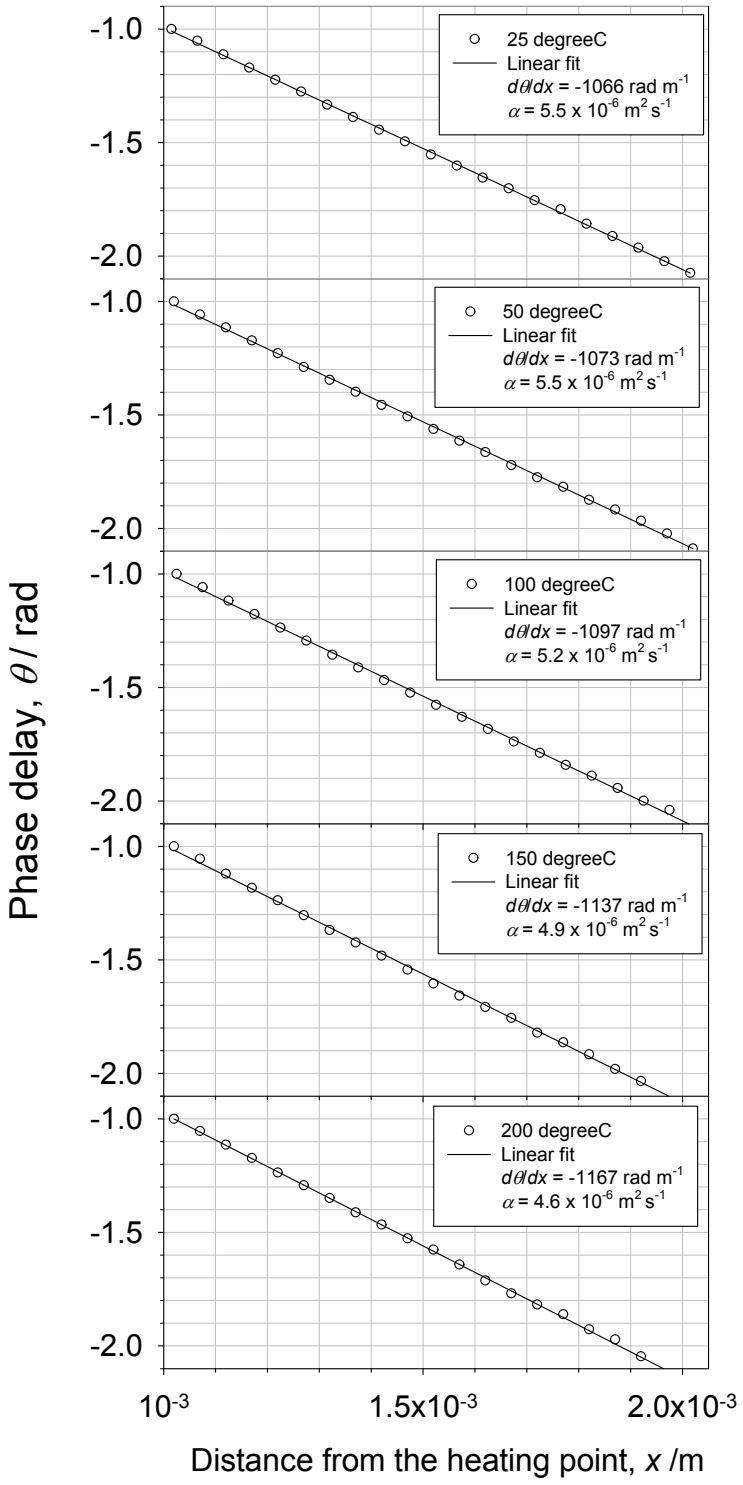

Figure S3. Relationship between the phase delay θ and distance from the heating point x for the Si-Mg_2Si ribbon at respective temperatures.

To verify our apparatus, we tested a certified reference material, BCR®-724C, Glass-ceramic distributed from European Commission, Joint Research Centre. We cut a BCR-724 rod into a thin disk shape with a thickness of 0.25 mm. Thin graphite layer was coated on both face of the disk in order to enhance thermal radiation and laser absorbance. Figure S4 shows measured data obtained at 20 degree C using a same manner for the Si-Mg_2Si ribbon. Measured thermal diffusivity was 1.91×10^{-6} m^2 s^{-1} and uncertainty of 95% confidence was 2.2%, which was in agreement with the reference value, 1.92×10^{-6} m^2 s^{-1} ±6.2% at 20 degree C.

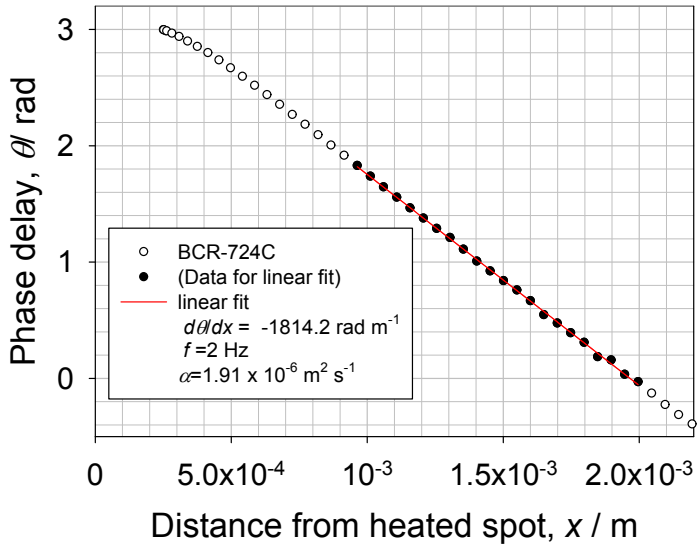

Figure S4. Relationship between phase delay of the temperature modulation and distance from heated spot for certified reference material, BCR-724C Glass-Ceramic. Thermal diffusivity was derived using the data for $10^{-3} < x < 2\times10^{-3}$ m according to Eq. S1.

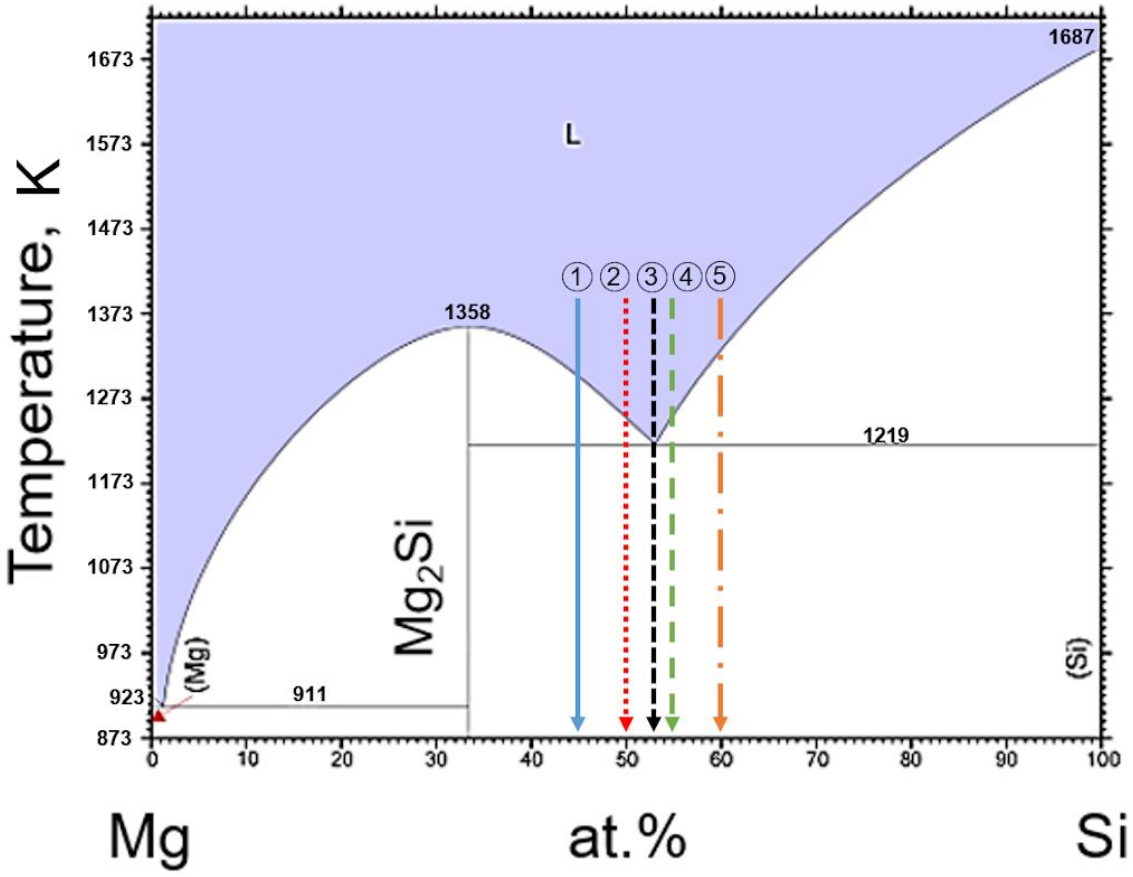

Figure S5. Mg-Si binary phase diagram. The labels 1, 2, 3, 4, and 5 correspond to Si:Mg_2Si = 39:61, 50:50, 56:44, 59:41, and 67:33, respectively.

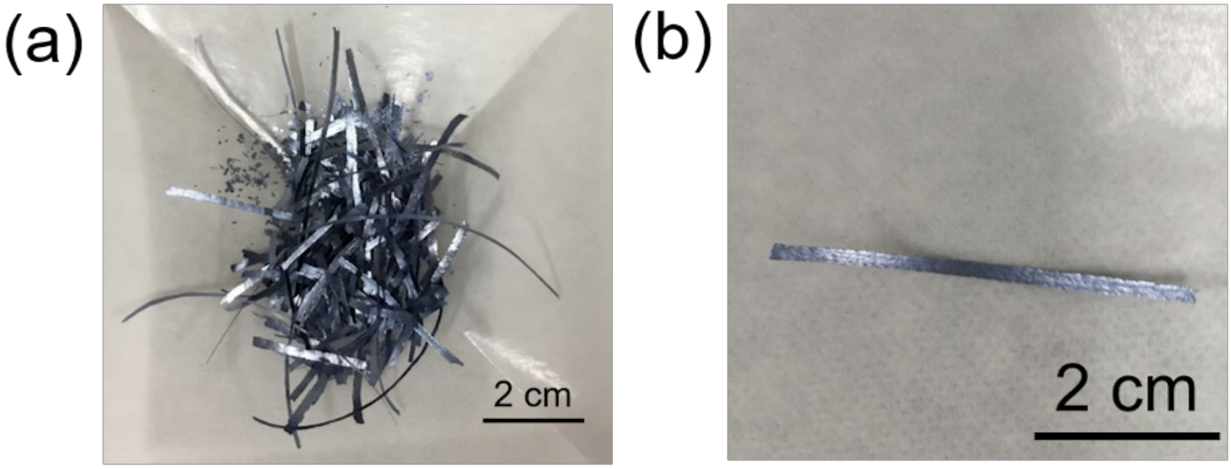

Figure S6. Appearance of synthesized ribbons for the (a) entire set of samples and (b) for a single sample.

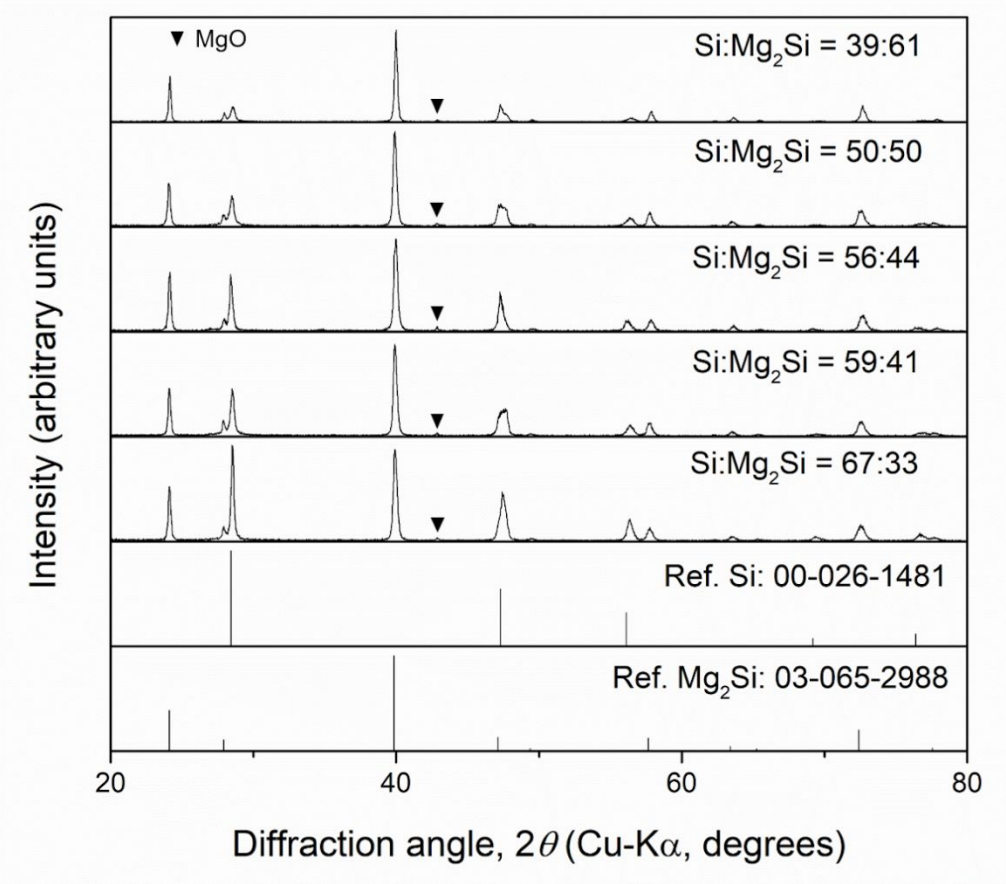

Figure S7. Powder X-ray diffraction (XRD) patterns of the Si-Mg_2Si nanocomposite ribbons, whereby the Bi content in Mg_2Si is fixed at x = 1.3 in (Mg_2Si + x at % Bi). The Si to Mg_2Si ratio varied as Si:Mg_2Si = 39:61, 50:50, 56:44, 59:41, and 67:33. The peak positions of pure Si and Mg_2Si are shown for comparison.

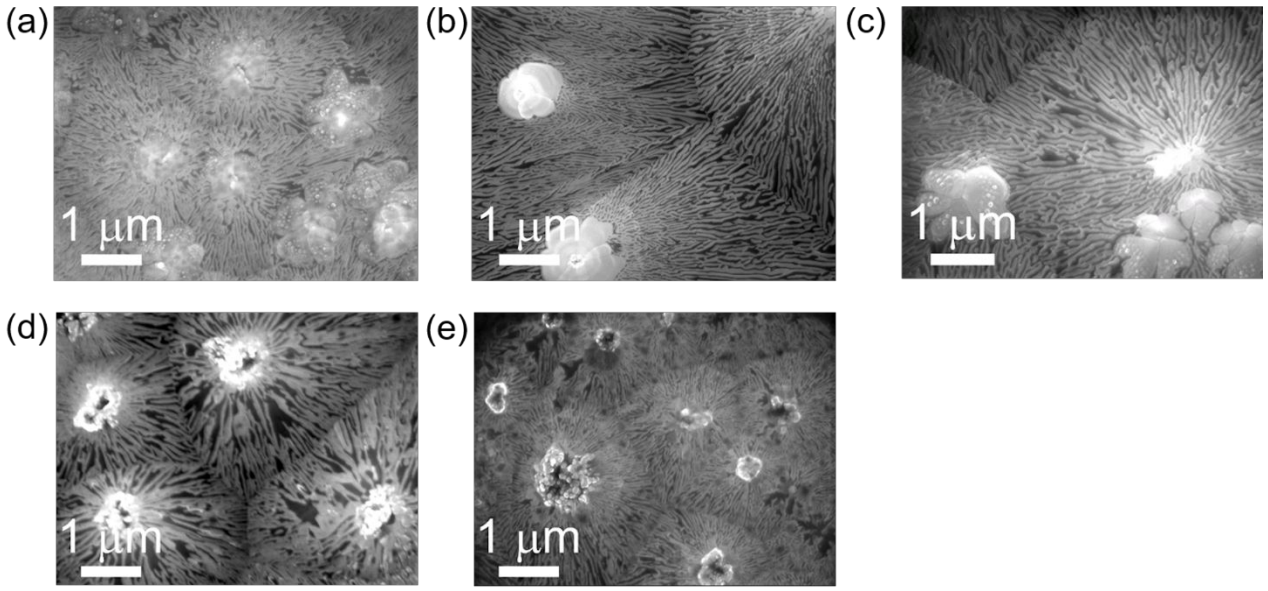

Figure S8. Scanning electron microscopy (SEM) images of the contact surface of the Si-Mg_2Si nanocomposite ribbons. The Bi content in Mg_2Si is fixed at x = 1.3 in (Mg_2Si + x at % Bi). (a), (b), (c), (d), and (e), correspond to 39:61, 50:50, 56:44, 59:41, and 67:33 in Si:Mg_2Si.

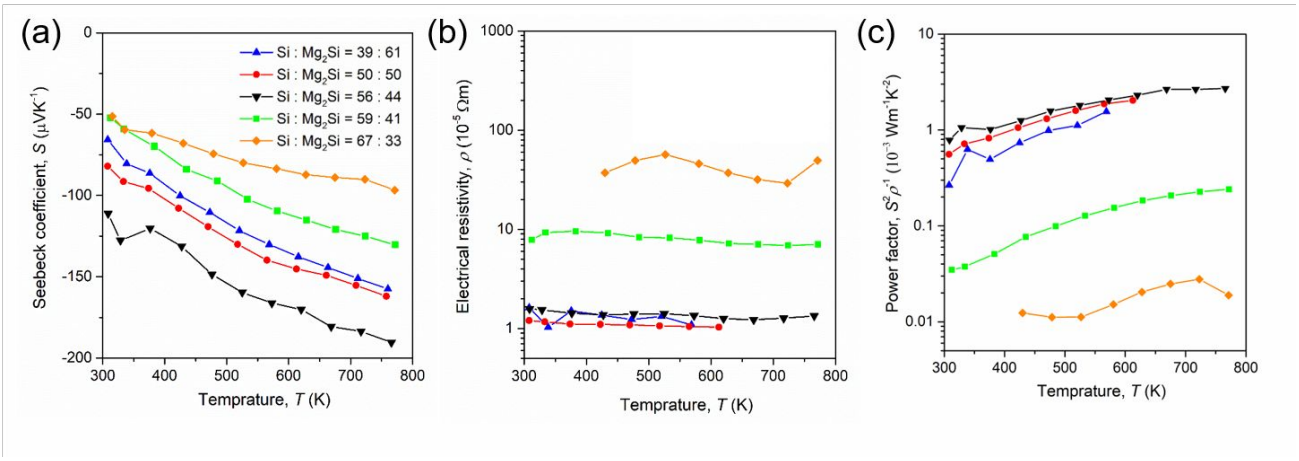

Figure S9. Temperature dependencies of (a) Seebeck coefficient S, (b) electrical resistivity ρ, and (c) power factor $S^2 \rho^{-1}$ of the Si-Mg_2Si nanocomposite ribbons, whereby the Bi content in Mg_2Si is fixed at x = 1.3 in (Mg_2Si + x at % Bi), and the Si to Mg_2Si ratio is varied according to Si:Mg_2Si = 39:61, 50:50, 56:44, 59:41, and 67:33.

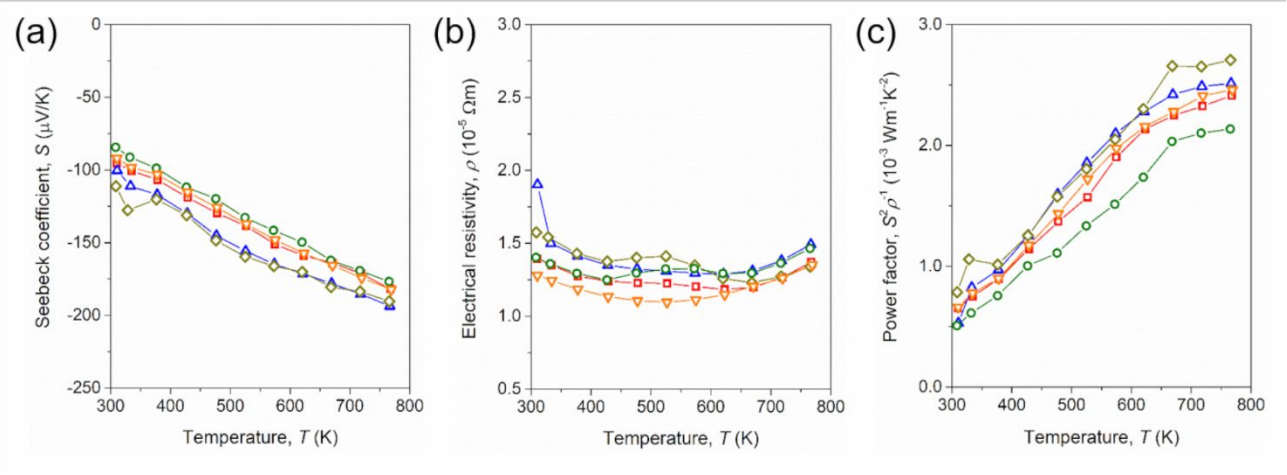

Figure S10. Temperature dependencies of (a) Seebeck coefficient S, (b) electrical resistivity ρ, (c) power factor $S^2 \rho^{-1}$ of a Si-Mg_2Si nanocomposite ribbon showing the best thermoelectric power factor. The Si to Mg_2Si ratio is 56:44 and the Bi content in Mg_2Si is x = 1.3 in (Mg_2Si + x at % Bi). Five ribbons are chosen from one sample batch at random for this characterization.

Table S1. Cubic lattice parameters (Si and Mg_2Si) of the Si-Mg_2Si nanocomposite ribbons, where the Si to Mg_2Si ratio is 56:44 and the Bi content in Mg_2Si is x = 1.3 in Mg_2Si + x at % Bi.

	Cubic lattice parameter	
Sample	Si (nm)	Mg_2Si (nm)
x = 0.3	0.5401	0.6376
x = 0.8	0.5405	0.6378
x = 1.3	0.5431	0.6356
x = 1.8	0.5405	0.6380
x = 2.5	0.5383	0.6382